Geophysical Journal International

Geophys. J. Int. (2022) **228,** 275–290
Advance Access publication 2021 August 27
GJI General Geophysical Methods

https://doi.org/10.1093/gji/ggab333

Desaturation effects of pyrite–sand mixtures on induced polarization signals

Tina Martin [1,*] Andreas Weller [2] and Laura Behling [3,*]

[1] *Lund University, Division of Engineering Geology, Lund,* 22363*, Sweden. E-mail: tina.martin@tg.lth.se*
[2] *Clausthal University of Technology, Institute of Geophysics, Clausthal-Zellerfeld,* 38678*, Germany*
[3] *Free University Berlin, Department of Earth Sciences, Berlin,* 12249*, Germany*

Accepted 2021 August 16. Received 2021 August 5; in original form 2021 March 18

SUMMARY

Induced polarization (IP) is an acknowledged method in ore exploration and can be applied to evaluate the metal content in dumps containing the residues of ore processing facilities. Existing models explain the relationships between ore content and grain size of the ore particles with IP parameters. However, the models assume full water saturation of the ore containing samples, which is often not the case in field conditions at dump sites. Hence, our study investigates the effect of desaturation on the resulting IP signal. We used six different sand–pyrite mixtures with varying amount and grain sizes of the pyrite particles. Evaporative drying desaturated the samples. Complex conductivity spectra were recorded in the frequency range between 0.02 and 1000 Hz at certain saturation levels. The resulting spectra indicate an decrease of the conductivity amplitude with progressing desaturation. This effect agrees with the second empirical Archie equation. The saturation exponent of the conductivity amplitude shows values slightly larger than one. The measured spectra were processed by a Debye decomposition. We observe a nearly constant total chargeability during desaturation. This finding is in agreement with existing models that relate the total chargeability to the metal content in the sample. However, the mean relaxation time decreases remarkably during the drying process, whereas the normalized relaxation time, which considers the ratio between the mean relaxation time and the resistivity of the embedding material, does not indicate any dependence on water saturation. This behaviour contradicts existing models that predict a decreasing relaxation time with increasing water salinity, which results from evaporative drying. In order to explain the observed effects, we propose a conceptional model that compares a mixture of pyrite particles in an embedding material (sand, water and air) with an electrical RC circuit. The pyrite grains behave as small condensers that are charged and discharged via the conductive background material. According to this simple physical model, the relaxation time is proportional to the resistivity of the embedding material. A resistivity increase while desaturation causes an increase of relaxation time as observed in our experiments. This conceptional model is in good agreement with other experiments that change the resistivity in the background material by varying water salinity or clay content. The capacitive behaviour of the dispersed particles is characterized by the normalized relaxation time that depends on the grain size and the volume content of the pyrite particles.

Key words: Electrical properties; Hydrogeophysics; Electromagnetic theory.

INTRODUCTION

The world's hunger for raw materials continues unabatedly. However, not only primary raw material sources are continuously being explored. Due to the increasing mineral ore prices also secondary mineral resources become more and more into the focus of investigation. One of the sources are historical mining dumps, which can still bear valuable mineral ore content since the mining and processing technology was not yet so advanced at the time of dumping. In addition, the interest in other metals than silver, lead, zinc, copper and iron ore was, for example, in these times not as big as today.

*Former: Federal Institute for Geosciences and Natural Resources, Berlin, Germany

© The Author(s) 2021. Published by Oxford University Press on behalf of The Royal Astronomical Society. This is an Open Access article distributed under the terms of the Creative Commons Attribution License (https://creativecommons.org/licenses/by/4.0/), which permits unrestricted reuse, distribution, and reproduction in any medium, provided the original work is properly cited.

Downloaded from https://academic.oup.com/gji/article/228/1/275/6358528 by Freie Universitaet user on 15 November 2021

Therefore, the interest in the exploration of abandoned mining dumps, which was the focus of the ROBEHA research project (Poggendorf *et al.* 2015; Kuhn & Meima 2019), is growing. Within this project, a variety of dumps has been investigated in the German Harz Mountains. Some of them contain fine-grained sand–mineral mixtures that originate from processing technologies using stamp mills in combination with oscillating tables.

Geophysical methods, and in particular geoelectrical techniques have proved to be suitable tools for the investigation of dumps with the residues of mining and processing activities (e.g. Grissemann *et al.* 2007; Rucker *et al.* 2009; Anterrieu *et al.* 2010; Placencia-Gomez *et al.* 2010; Martin-Crespo *et al.* 2011; Martin *et al.* 2020). The application of the induced polarization (IP) method, which is an extension of the conventional resistivity technique, provides additional potential of ore minerals, which are characterized by high polarization effects (e.g. Bleil 1953; Van Voorhis *et al.* 1973; Pelton *et al.* 1978; Revil *et al.* 2015a; Martin *et al.* 2021).

Usually, different moisture conditions occur at the dumps depending on their location, the cover, the meteorological conditions and the hydrologic situation. In any case, the water saturation is varying, and full saturation is rare. However, most laboratory experiments on sand–mineral mixtures have been conducted with fully water saturated samples (e.g. Hupfer *et al.* 2016). Unfortunately, only few studies investigated the influence of desaturation on the IP signal in natural material. For example, Ulrich & Slater (2004) reported significant changes in the polarization magnitude during evaporative drying and pressure drainage on unconsolidated sand samples. Kruschwitz (2008) and Zhang *et al.* (2019) observed similar effects while desaturating their sandstone samples. In addition, Martin (2010) describes the changes in the IP quantities for moisture changes in wood samples.

To the best of our knowledge, only one study has been published that reports the desaturation of artificial mixtures with electronically conducting particles. Tartrat *et al.* (2019) investigate the effect of saturation upon the complex conductivity of mixtures of pyrite, water and illitic clay as background material. The moderate chargeability of the background material is a special feature of their experiments and a challenge for interpretation.

In continuation to the experiments of Hupfer *et al.* (2016), we investigate the effect of desaturation of synthetic mixtures consisting of pyrite, water, and sand as background material. In contrast to the experiments of Tartrat *et al.* (2019), the sand causes only a vanishing polarization. We prepared different mixtures with varying pyrite content and grain size and recorded the IP spectra at different saturation levels during the evaporative drying process. We compare the findings of our experiment with the prediction of the mechanistic model of Tartrat *et al.* (2019). This model is based on a previous approach of Revil *et al.* (2015a) that attributes the IP relaxation to the diffusion of the charge carriers inside the metallic particles. We propose an alternative model that is based on a RC circuit. The IP relaxation corresponds to a discharge of the condenser-like metallic particles via the electrical resistivity of the embedding material.

THEORY

Our study investigates the changes in the electrical properties of sand–pyrite mixtures while evaporative drying. The drying process causes a reduction of the volume of water V_w in the pore space. The water saturation S_w describes the ratio between the volume of water and the total volume of the pore space V_p

$$S_\mathrm{w} = \frac{V_\mathrm{w}}{V_p}. \tag{1}$$

The effect of drying, which replaces a conductive fluid by non-conducting air, is related to a decrease in the conductivity of the porous medium. Assuming a conductivity σ_o for a fully saturated sample and a conductivity σ_p of the partially saturated sample ($S_\mathrm{w} < 1$), the second Archie equation formulates a power law dependence between σ_p and S_w:

$$\sigma_p\,(S_\mathrm{w}) = \sigma_\mathrm{o} S_w^n, \tag{2}$$

with n being the saturation exponent (e.g. Schön 2011). However, with evaporative drying the pore water conductivity increases with decreasing saturation as $\sigma_\mathrm{o}/S_\mathrm{w}$. Thus, we can replace σ_0 by $\sigma_\mathrm{o}/S_\mathrm{w}$ and instead of eq. (2) we have:

$$\sigma_p\,(S_\mathrm{w}) = \sigma_\mathrm{o} S_w^{n-1} = \sigma_o S_\mathrm{w}^{n_{ev}}, \tag{3}$$

with $n_\mathrm{ev} = n$–1 being the saturation exponent resulting from evaporative drying (e.g. Tartrat *et al.* 2019; Zhang *et al.* 2019). This formulation is valid for the conductivity amplitude. However, the conductivity of soils and rocks, which includes conduction and polarization effects, can be generally represented by a complex conductivity $\sigma*$, (or complex resistivity $\rho* = 1/\sigma*$). The complex conductivity is expressed in terms of magnitude $|\sigma|$ and phase angle φ, or by real (σ') and imaginary (σ'') components,

$$\sigma^* = |\sigma^*| \cdot e^{i\varphi} = \sigma' + i\sigma'', \tag{4}$$

with $i = \sqrt{-1}$ being the imaginary unit, and

$$\tan(\varphi) = \frac{\sigma''}{\sigma'}, \tag{5}$$

$$|\sigma^*| = \sqrt{\sigma'^2 + \sigma''^2} = \frac{1}{|\rho^*|}. \tag{6}$$

The spectral induced polarization (SIP) method considers the frequency dependence of the complex conductivity $\sigma*(f)$ or complex resistivity $\rho*(f)$ with f being the frequency in Hz. The spectra of complex conductivity measured over a wide frequency range provide insight into the conduction and polarization processes of porous material.

A Debye decomposition approach (Nordsiek & Weller 2008) has proved to be a useful tool to extract valuable parameters from the measured complex conductivity spectra. This method is used to recover characteristic parameters like DC resistivity, total chargeability, and mean relaxation time. With this approach, the frequency-dependent complex electrical resistivity $\rho*(f)$ describes an IP spectrum that can be fitted by a superposition of k Debye terms

$$\rho^*(f) = \rho_0 \left(1 - \sum\nolimits_{j=1}^{k} m_j \left(1 - \frac{1}{1 + i2\pi f \tau_j}\right)\right), \tag{7}$$

with ρ_0 being the direct current (DC) resistivity, m_j and τ_j are pairs of partial chargeability and relaxation time of a single Debye model. The k chargeability values m_j, which are related to a set of predefined relaxation times τ_j, and the value of DC resistivity ρ_0 are the result of a fitting procedure as described by Nordsiek & Weller (2008). To compress the number of parameters, we determine the integrating parameters total chargeability

$$m_t = \sum_{j=1}^{k} m_j, \tag{8}$$

Downloaded from https://academic.oup.com/gji/article/228/1/275/6358528 by Freie Universitaet user on 15 November 2021

and mean relaxation time

$$\tau_{\text{mean}} = \exp\left(\frac{\sum_{j=1}^{k} m_j \ln(\tau_j)}{m_t}\right). \tag{9}$$

The ratio between total chargeability and electrical resistivity provides an additional parameter that is called normalized chargeability:

$$m_n = \frac{m_t}{\rho} = m_t\sigma, \tag{10}$$

which presents the net polarization effect independent of the resistivity. The normalized chargeability is similar to the metal factor that multiplies conductivity and frequency effect (Lesmes & Frye 2001). For mixtures with electronically conducting (metallic) particles, the conductivity spectra indicate remarkable difference between high- and low-frequency conductivity. The addition of metallic particles in sand mixtures causes a decrease of conductivity at low frequencies and an increase at high frequencies (e.g. Revil *et al.* 2015a). Therefore, we use for σ in eq. (10) the geometric mean of high- and low-frequency values of conductivity σ_{gm}. This value is assumed to be the conductivity of the background material.

According to Slater *et al.* (2005), the normalized relaxation time is defined as the ratio between mean relaxation time and resistivity

$$\tau_n = \frac{\tau_{\text{mean}}}{\rho} = \tau_{\text{mean}}\sigma. \tag{11}$$

It should be noted that the physical unit of τ_n, which is As/Vm or F/m, corresponds formally to the dielectric permittivity.

A variety of studies use Cole–Cole type models for the determination of special parameters that characterize the IP spectra (e.g. Pelton *et al.* 1978; Revil *et al.* 2015a; Hupfer *et al.* 2016; Tartrat *et al.* 2019). The application of Cole–Cole type models is restricted to a certain behaviour of the measured complex conductivity spectra. They provide good fitting results for phase spectra with a symmetric accentuated phase peak. The Debye decomposition proves to be more flexible and stable for complicated spectra that cannot be fitted by simple Cole–Cole type models (Nordsiek & Weller 2008).

Beside the Debye decomposition, we used in our study a double Pelton model as proposed by Pelton *et al.* (1978):

$$\rho^*(f) = \rho_0\left[1 - m_P\left(1 - \frac{1}{1 + (i2\pi f\tau_P)^c}\right)\right] \times \left[\frac{1}{1 + (i2\pi f\tau_E)^{c_E}}\right], \tag{12}$$

with ρ_0 being the DC resistivity, m_P the chargeability, τ_P the time constant, and c the so-called Cole–Cole exponent. The term in the second square bracket considers the high-frequency dispersion effects with time constants τ_E typically in the range between 10^{-8} s and 10^{-12} s. The high-frequency Cole–Cole exponent c_E and the time constant τ_E are ignored in the further spectral analysis.

The origin of the electrical relaxation of charged metallic particles embedded in a porous conducting medium has been discussed for more than five decades (e.g. Wong 1979; Revil *et al.* 2015a; Gurin *et al.* 2019; Tartrat *et al.* 2019) without providing a model that proves to be fully compatible with all experimental observations.

It is widely agreed that the total chargeability is a good proxy for the estimation of the volume fraction of metallic particles p_v. Considering the theory of Wong (1979), Gurin *et al.* (2015) propose a relationship between p_v and m_t that considers the chargeability of the background material m_m:

$$m_t = 1 - (1 - m_m)\frac{2(1 - p_v)^2}{(2 + p_v)(1 + 2p_v)}. \tag{13}$$

In absence of background chargeability, a simplified version predicts a linear relationship (Revil *et al.* 2015a):

$$m_t = \frac{9}{2}p_v. \tag{14}$$

Additionally, Revil *et al.* (2015a) propose a linear relationship between p_v and the maximum of the phase spectrum:

$$\varphi_{\max} \approx \frac{9}{4}p_v. \tag{15}$$

More discussion is related to the relaxation time τ that describes the temporal voltage decay of a charged metallic particle. The basic equation reads (e.g. Gurin *et al.* 2013; Revil *et al.* 2015a)

$$\tau = \frac{r^2}{D}, \tag{16}$$

where r is the radius of the metallic particle and D the apparent diffusion coefficient of the charge carriers responsible for the polarization of the particle. There is a variety of methods to determine the relaxation time τ. The simplest way is the extraction from the maxima of the phase spectrum or spectrum of the imaginary conductivity. Other approaches use the time constant of Cole–Cole type models or the mean relaxation time from Debye decomposition procedures applied to time or frequency domain data. It should be noted that the different time constants or relaxation times might differ considerably. These differences complicate the comparison of parameters originating from different studies.

A proportionality between τ and r^2 as indicated in eq. (16) has been assumed in the theories that consider the diffusion of the charge carriers as the origin of polarization effects (e.g. Schwarz 1962; Gurin *et al.* 2013; Revil *et al.* 2015a). Thus, the significance and size of the apparent diffusion coefficient D has been widely discussed. The theory of Revil *et al.* (2015a) attribute the main diffusion process to the charge carriers inside the metallic particles. However, this theory is not able to explain the observed inverse relationship between relaxation time and water resistivity ρ_{w} (e.g. Slater *et al.* 2005; Gurin *et al.* 2015; Hupfer *et al.* 2016). Considering this relationship, Gurin *et al.* (2015) formulate:

$$\tau = ar^2\rho_w, \tag{17}$$

where the coefficient a (with the dimension F m^{-3}) defines a volumetric specific capacitance. This formulation suggests that the relaxation time is controlled by the capacitance of the metallic particles and the conductivity of the embedding liquid. A further generalization replaces ρ_{w} by the conductivity of the embedding porous material ρ_b resulting in:

$$\tau = a^*r^2\rho_b, \tag{18}$$

with a^* being a modified specific capacitance. Tartrat *et al.* (2019) propose a similar equation with a special definition of the modified specific capacitance:

$$a^* = \frac{e^2C_m}{k_bT}, \tag{19}$$

where e denotes the elementary charge (1.6×10^{-19} C), C_m the concentration of charge carriers in the solid metallic particle (m^{-3}), k_b the Boltzmann constant (1.38×10^{-23} m^2 kg s^{-2} K^{-1}) and T the absolute temperature (K).

Downloaded from https://academic.oup.com/gji/article/228/1/275/6358528 by Freie Universitaet user on 15 November 2021

Conceptional model

Regarding eq. (18), the parameter $c_s = a^* \times r^2$ controls the capacitive behaviour of metallic particles,

$$\tau = c_s \rho_b. \tag{20}$$

The parameter c_s (in F m^{-1}) corresponds to the normalized relaxation time τ_n with the unit F m^{-1} as defined in eq. (11) and considering $\rho_b = \rho$ as sample resistivity. Eq. (20) corresponds to the idea of Pelton *et al.* (1978) to describe the electrical behaviour of a mixture of conductive particles embedded in a rock matrix by a *RC* circuit, which is composed of a serially connected resistor (R_1) and a capacitor (C) connected in parallel with another resistor (R_0) (see their fig. 1b). The relaxation time of a *RC* circuit is

$$\tau = RC, \tag{21}$$

with $R = R_0 + R_1$ in the case of the Pelton model. Considering a rock, the resistance has to be replaced by the background resistivity ρ_b (in Ωm) and the capacity by a 'specific capacitance' c_s as formulated in eq. (20). Obviously, the parameter $c_s = \tau_n$ characterizes the capacitive behaviour of the metallic particles. We assume that the conductive particles, which might be considered as spherical capacitors, are embedded in a material with a uniform resistivity ρ_b. The capacitors are charged and discharged via current flow through the embedding material. Eq. (20) presents a purely physical approach. It considers neither electrochemical reactions on the surface of the metallic particle nor a diffusion inside the particle.

Assuming that the capacity of the conductive particles is independent on the resistivity of the embedding material, the relaxation time depends only on the resistivity of the material ($\tau \sim \rho_b$). Porosity, mineral composition, water salinity, water saturation and temperature control the resistivity of the embedding material.

In our study, we verify the proposed model using existing experimental findings and new data of desaturation experiments with pyrite–sand mixtures. We investigate the saturation dependence of σ_{gm}, σ''_{max}, m_t, m_n, τ_{mean}, τ_n and the Cole–Cole exponent c.

MATERIAL AND METHODS

Sample holder and instrument

A four-point measurement cell was developed for unconsolidated material (Fig. 1a; for details see Hupfer *et al.* 2016). The sample holder consists of three parts: one central part with the material and enclosed with glass frits as well as two outer containers, which contain the coupling fluid and the stainless-steel plate electrodes.

At the central part, four potential taps are located as pairs in the middle of the sample holder, facing opposite sides (Fig. 1a). The potential taps are made of tensiometer tips with a porous ceramic at the top and a silver wire immersed in an aqueous solution (0.1 mol l^{-1} NaCl). This design avoids electrode polarization at the potential taps.

The SIP measurements were carried out using the high-accuracy impedance spectrometer SIP-ZEL (Zimmermann *et al.* 2008). This instrument enables measurements of the impedance in a frequency range from 1 mHz to 45 kHz with an accuracy of 0.1 mrad at frequencies below 1 kHz. It records the magnitude and the phase of the impedance based on the time series of the injected current and measured voltage. Considering the geometric factor of the sample holder, the measured impedance is transformed into resistivity amplitude and phase, and finally in real and imaginary part of conductivity.

Due to two amplifiers, either the measurements of two samples can be performed or the measurement of two pairs of potential electrodes in parallel as conducted in this study (Fig. 1b). The measurements took place in a climate chamber (at constant temperature of 20 °C) to avoid any temperature effects (Fig. 1b).

Samples

In this study, we investigated six unconsolidated samples, mixed of cleaned pyrite of varying grain sizes (grain radius 56–1000 μm) and pure quartz sand (grain radius 56–178 μm, Fig. 1c). We prepared mixtures with a single pyrite grain radius in sand and mixtures with two different grain radii in a sand matrix (Fig. 1c). The pyrite mineral content of the mixtures with a single pyrite grain radius was 2.75 vol. per cent. The mixtures with two pyrite grain radii were composed of 2.75 vol. per cent of the lower pyrite grain radius fraction and additional 2.75 vol. per cent of the larger pyrite grain radius resulting in a volume percentage of 5.50 per cent (Table 1). The sample SP 04 includes two neighbouring pyrite grain radii ranging from 315 to 1000 μm. Therefore, we consider this sample also as mixture with a single pyrite grain radius throughout the manuscript. We have assigned the samples with a single pyrite grain radius to sample set 1 (SP 01, SP 02 and SP 04), whereas sample set 2 includes the samples with two separated pyrite grain radii (SP 05, SP 06 and SP 07). We investigate with the sample set 1 the effect of pyrite grain radius on saturation and with set 2 the influence of the varying width of the pyrite grain radii distribution.

The samples were always prepared with the same procedure to ensure reproducible and comparable results. The cross-riffling-method was applied to homogenize the samples. The homogeneous mineral–quartz–sand mixture was packed in the sample holder stepwise, adding water (0.01 mol l^{-1} NaCl) for each respective step until the sample holder was fully filled. Considering our recipe of packing procedure, we assume that nearly full saturation was achieved.

In a preceding experiment, a pure sand sample was used to determine the electrical properties of the background material. The resulting spectra for the fully saturated sample indicate a nearly constant resistivity of 22 Ωm and phase values close to the limit of resolution of the equipment (<0.1 mrad) in the frequency range <100 Hz. A total chargeability of 0.01 has been determined for the sand sample.

Desaturation

After the initial SIP measurement on the fully saturated samples, the outer containers with coupling fluid were removed and the desaturation took place via evaporation at room temperature through the glass frits and the four openings for the potential taps. The drying process starts from the margin and progresses to the inner parts of the sample. Therefore, we get an inhomogeneous saturation distribution in the sample. We assume that the saturation inhomogeneity is balanced by the impedance measurements that provides an integral value considering all the sample volume. Therefore, the resulting saturation reflects a mean value corresponding to the sample size.

The desaturation process was monitored every day through weighing. The observed weight loss, which is attributed to the evaporated water, was approximately 2 g d^{-1}. Knowing the pore volume V_p and the current volume of water in the sample V_{w}, the water saturation S_w is calculated by eq. (1).

Downloaded from https://academic.oup.com/gji/article/228/1/275/6358528 by Freie Universitaet user on 15 November 2021

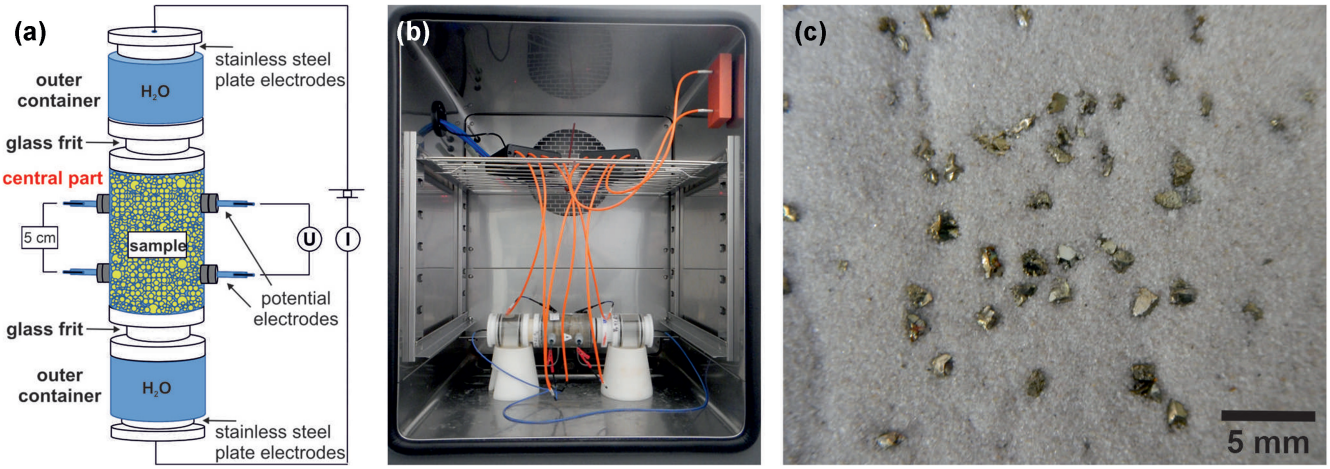

Figure 1. Sample holder and material. (a) Sample holder for unconsolidated material. (b) Measurement in the climate chamber. (c) Pyrite in sand.

Table 1. Overview about the measured samples: grain radii and pyrite content.

Sample	Set	First pyrite grain radius [μm]	Second pyrite grain radius [μm]	Mean pyrite grain radius r_{gm} [μm]	Pyrite content p_v [vol. per cent]
SP 01	1	56–100	-	75	2.75
SP 02	1	100–315	-	177	2.75
SP 04	1	315–500	500–1000	561	5.50
SP 05	2	177–315	500–1000	421	5.50
SP 06	2	100–177	500–1000	316	5.50
SP 07	2	56–100	500–1000	236	5.50

In a 3-to-7-day rhythm, the sample holder was reassembled, and a new SIP measurement was conducted. To calculate the saturation and to check potential undesired resaturation processes, each sample was weighted before and after the measurement. We observed a slight increase of water saturation during the SIP measurement. It could not be avoided that a small amount of water intruded from the outer water containers via the porous glass frits into the sample. To minimize this partial resaturation, the measurement time was kept as short as possible. Preliminary investigation of the permeability of glass frits revealed a duration of approximately 20 min for passing the fluid through the glass frits. In addition, the results in Hupfer *et al.* (2016) on pyrite–sand mixtures suggested, that the IP effect is observed mainly at frequencies larger than 1 Hz. Therefore, we have chosen a narrower frequency range between 20 mHz and 1000 Hz that could be recorded in only 20 min.

RESULTS

Complex conductivity spectra

Fig. 2 displays the complex conductivity spectra for all samples at full water saturation. Sample SP 07 shows the highest conductivities (80 mS m^{-1} at low frequency) in both conductivity amplitude (a) and real part of conductivity (c), whereas sample SP 02 shows the lowest values (40 mS m^{-1} at low frequency). Though the same recipe of preparation has been used for all samples, variations in the resulting low-frequency conductivity could not be excluded. We attribute these variations to small differences in the final fluid salinity caused by dissolution of impurities in the pyrite or sand fraction.

It is also obvious that the conductivity increases with increasing frequency for all samples but with different shape. The spectra of phase (b) and imaginary part of conductivity (d) indicate a clear maximum for all samples. Considering eq. (15), the amplitude of the phase maxima should be related to the volumetric content of pyrite particles. We observe the lowest phase maximum with 54.4 mrad for the sample SP 02 with low pyrite content. The phase maxima of the samples with $p_v = 5.5$ vol. per cent vary between 79.6 and 85.7 mrad.

In contrast to all other samples that indicate a single maximum, a second peak can be surmised for sample SP 07 by the asymmetric hunch at a frequency of about 200 Hz. The spectra for the desaturation experiment of sample SP 02 are shown as an example for the samples with a single grain radius (set 1) in Fig. 3, whereas Fig. 4 displays the spectra of sample SP 05 with two separate pyrite grain radii (set 2). It can be observed in both figures that with decreasing saturation, both the conductivity amplitude (a) and the real part of conductivity (c) decreases. Furthermore, the maxima of the conductivity phase (b) and the imaginary conductivity (d) decrease with decreasing saturation. Additionally, the peak frequency is shifted to lower frequencies up to more than two orders of magnitude.

In general, the conductivity amplitude is very similar to the real part of conductivity. Therefore, we consider only the conductivity amplitude for further analysis.

For some of the measurements (e.g. Fig. 3: $S_w = 0.35$, Fig. 4: $S_w = 0.36$), a strong phase increase is observed for frequencies larger 3 kHz. We attribute this effect to electromagnetic (EM) coupling effects. However, we use eq. (12) to quantify the EM effects by the second Pelton-term. Since we remove the EM effect for the subsequent data processing, the resulting Debye parameters are not affected by the high frequency distortions.

Downloaded from https://academic.oup.com/gji/article/228/1/275/6358528 by Freie Universitaet user on 15 November 2021

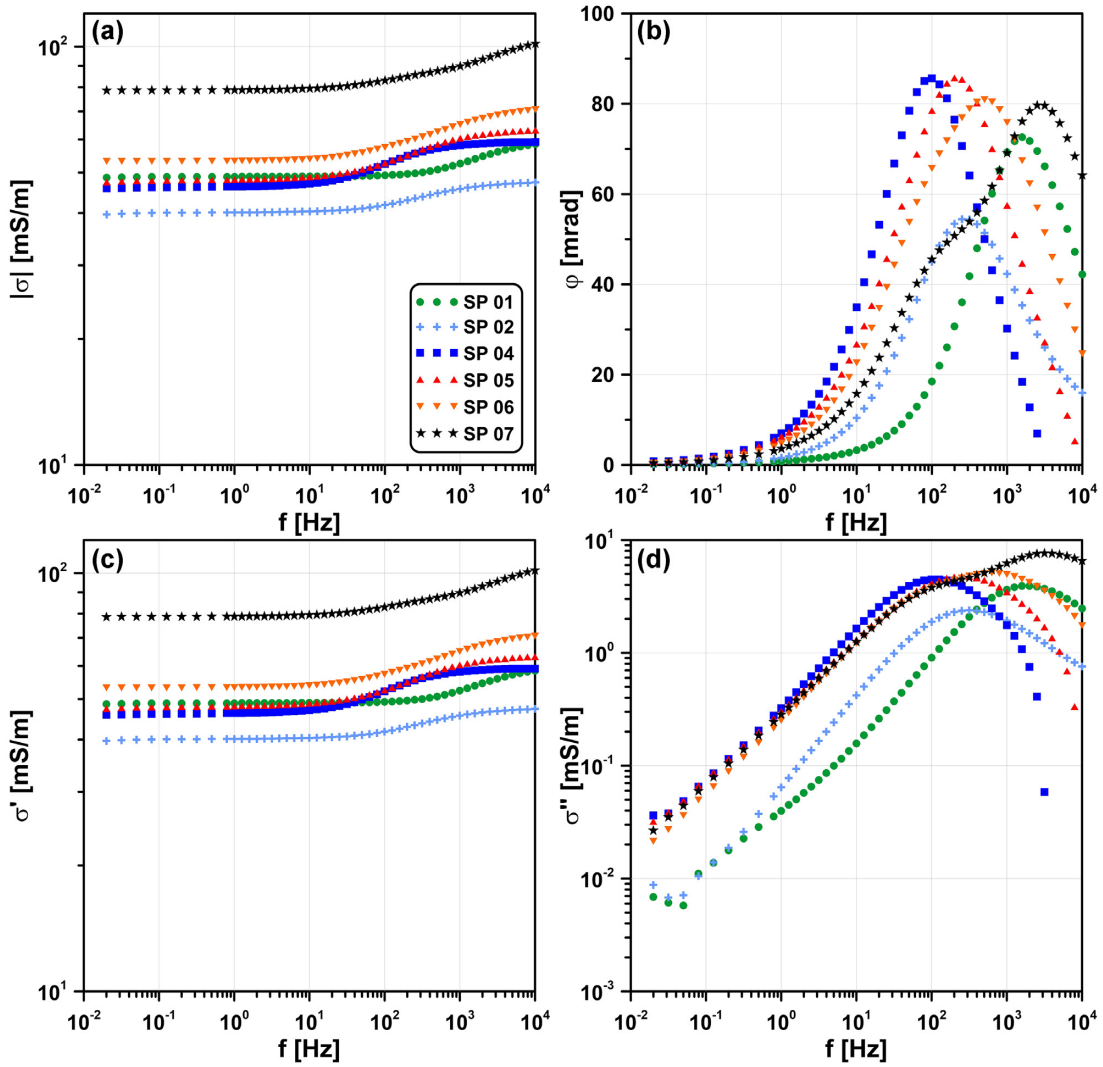

Figure 2. IP spectra for all samples at full water saturation. (a) Conductivity amplitude. (b) Phase of conductivity. (c) Real part of conductivity. (d) Imaginary part of conductivity.

Conductivity amplitude

In general, the conductivity amplitude increases with frequency. Only for very low frequencies the amplitudes start to increase for some samples due to the starting unwanted resaturation during the measurement time of 20 min. We selected the geometric mean value of the low and high frequency limits of conductivity. In order to compare the saturation dependence of the different samples, we normalized the conductivity amplitude to the value acquired at full water saturation. Fig. 5 displays the saturation dependence of normalized conductivity as a function of water saturation in a double logarithmic plot. The slope of the fitting lines, which are forced to pass through the origin, reflect the saturation exponent n_{ev} as defined in eq. (3). The saturation exponents vary in a narrow range between 1.05 and 1.32.

Maximum of imaginary part of conductivity

In Fig. 6, the normalized maximum of the imaginary part of conductivity is shown as a function of saturation in a double logarithmic plot in accordance with the presentation in Fig. 5. Considering the slope of the fitting line, a saturation exponent can be determined. We name the saturation exponent of the imaginary part of conductivity p_{ev}. The resulting values of the saturation exponent p_{ev} vary between 1.27 and 1.77.

Parameters of Debye decomposition

The Debye decomposition of the resulting spectra was performed for each sample and at each desaturation step. Figs 7 to 10 display the saturation dependence of the resulting parameters: the total chargeability m_t, the normalized chargeability m_n, the mean relaxation time τ_{mean}, and the normalized relaxation time τ_n.

Total chargeability

For most samples, the total chargeability m_t only slightly decreases with decreasing saturation as shown in Fig. 7. Samples SP 02 and SP 07 indicate a nearly constant behaviour. The chargeability values differ between 0.13 and 0.31 while the exponent a_1 of the fitting power law varies between –0.01 and 0.16.

Downloaded from https://academic.oup.com/gji/article/228/1/275/6358528 by Freie Universitaet user on 15 November 2021

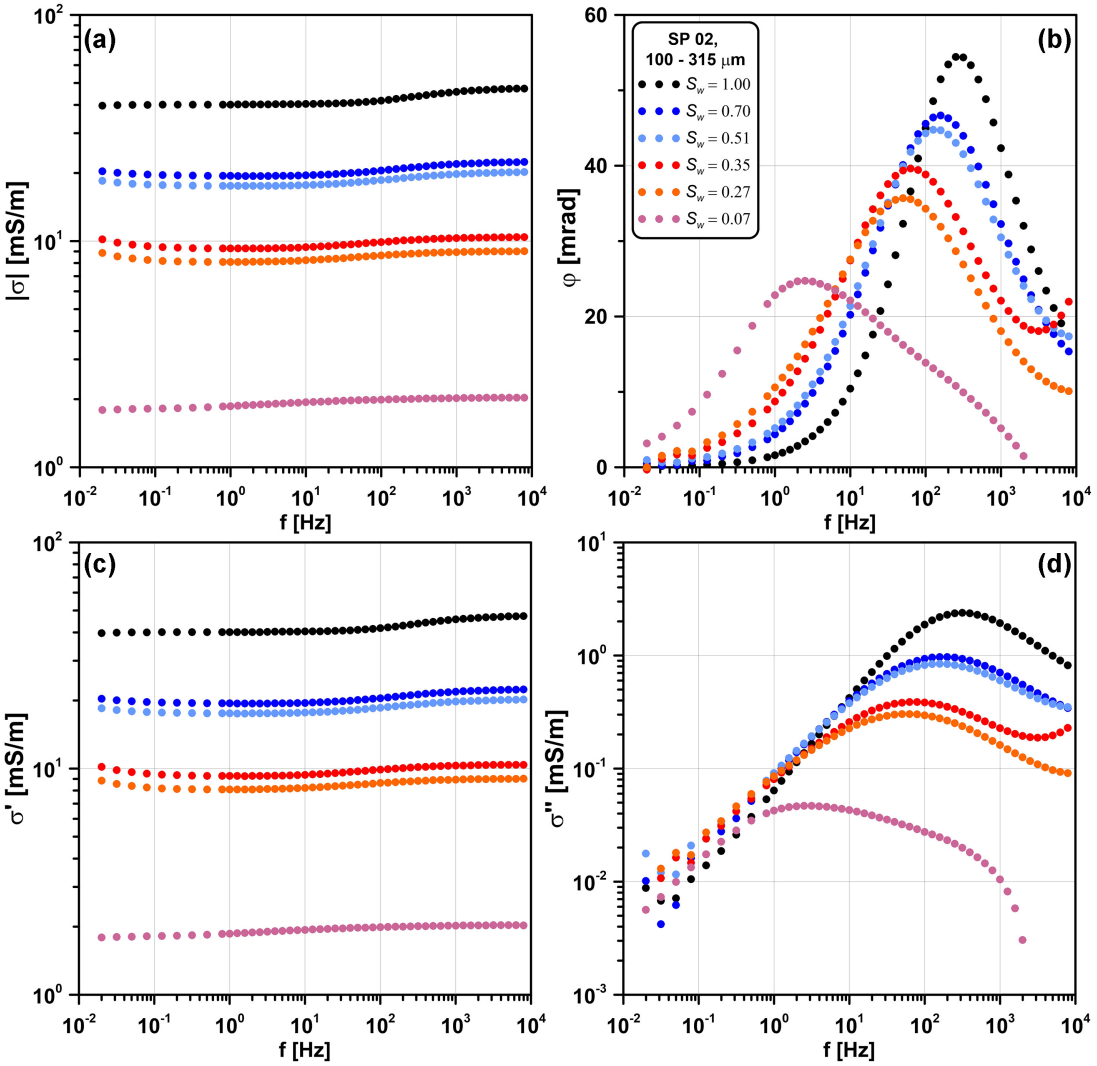

Figure 3. IP spectra for set 1 sample SP 02 for different values of water saturation. (a) Conductivity amplitude. (b) Phase of conductivity. (c) Real part of conductivity. (d) Imaginary part of conductivity.

Normalized chargeability

A significant decrease of the normalized chargeability m_n with gradually drying can be observed in Fig. 8 for all samples. We find only small changes in the power-law exponent a_2, which describes the saturation dependence of normalized chargeability. Sample SP 01 indicates with $a_2 = 1.43$ the largest saturation exponent.

Mean relaxation time

The mean relaxation time of the fully saturated mixtures varies between 0.1 and 2.3 ms. We observe in Fig. 9 a significant increase of the mean relaxation time during the evaporative drying of all samples. The exponent a_3 of the fitting power law, which corresponds to the slope of the fitting line in the double logarithmic plot, varies between –0.90 for sample SP 04 and –1.63 for samples SP 01.

Normalized relaxation time

We observe in Fig. 10 that the normalized relaxation time τ_n does not show any significant dependence on water saturation. Instead, a rather constant value was derived for each sample. Only sample SP 07 shows higher variation, which might be caused by the lower data quality.

Quantities of the measured IP spectra and the integrating parameters of the Debye decomposition for the samples at full saturation can be found in Table 2. The resulting power-law fitting exponents are compiled in Table 3.

Parameters of the Pelton model

The complex conductivity spectra of sample set 1 indicate a Cole–Cole like behaviour. The phase spectra display an accentuated phase peak as shown in Fig. 3(b). Similar phase spectra are observed for samples SP 05 (see Fig. 4b) and SP 06. The double Pelton model has been applied in a fitting procedure to determine the parameters DC resistivity, chargeability m_P, the time constant τ_P, and the Cole–Cole exponent c. However, the double Pelton model could not reliably fit the spectra of sample SP 07 with the widest grain size distribution (see Fig. 2) that causes a distorted phase spectrum. The resulting parameters for the fully saturated samples are compiled in Table 2.

Downloaded from https://academic.oup.com/gji/article/228/1/275/6358528 by Freie Universitaet user on 15 November 2021

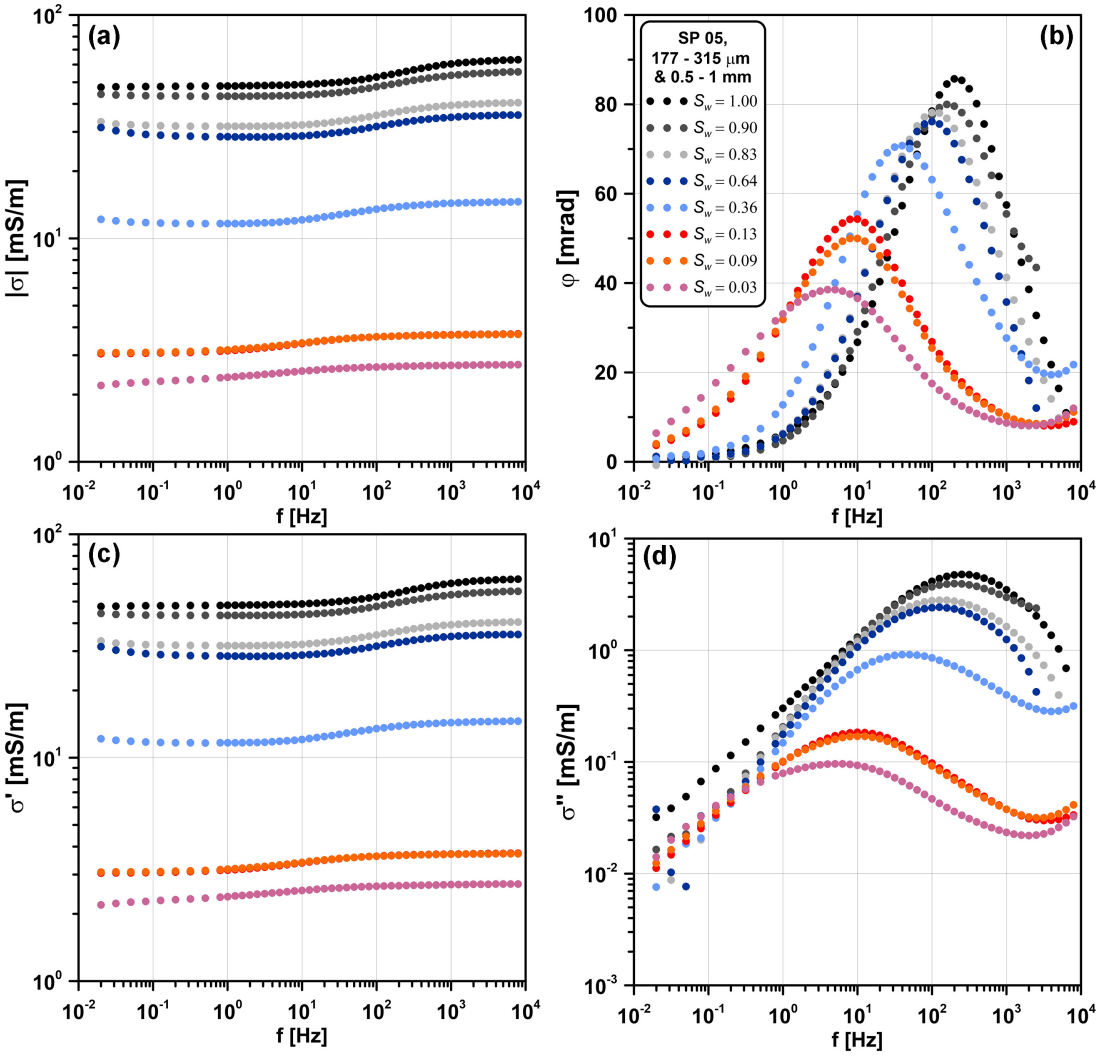

Figure 4. IP spectra for set 2 sample SP 05 for different values of water saturation. (a) Conductivity amplitude. (b) Phase of conductivity. (c) Real part of conductivity. (d) Imaginary part of conductivity.

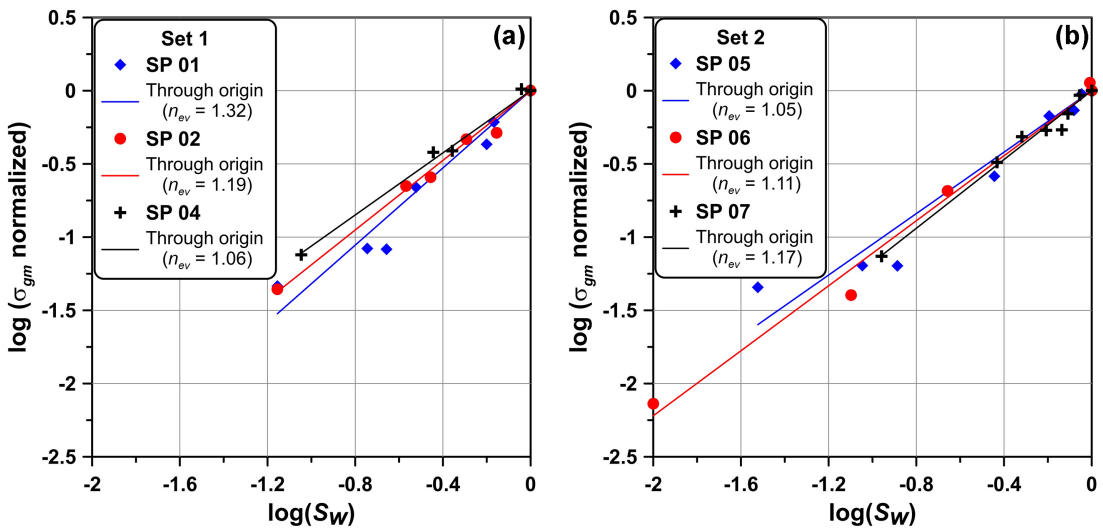

Figure 5. Normalized conductivity as function of saturation for (a) set 1 samples and (b) set 2 samples.

Downloaded from https://academic.oup.com/gji/article/228/1/275/6358528 by Freie Universitaet user on 15 November 2021

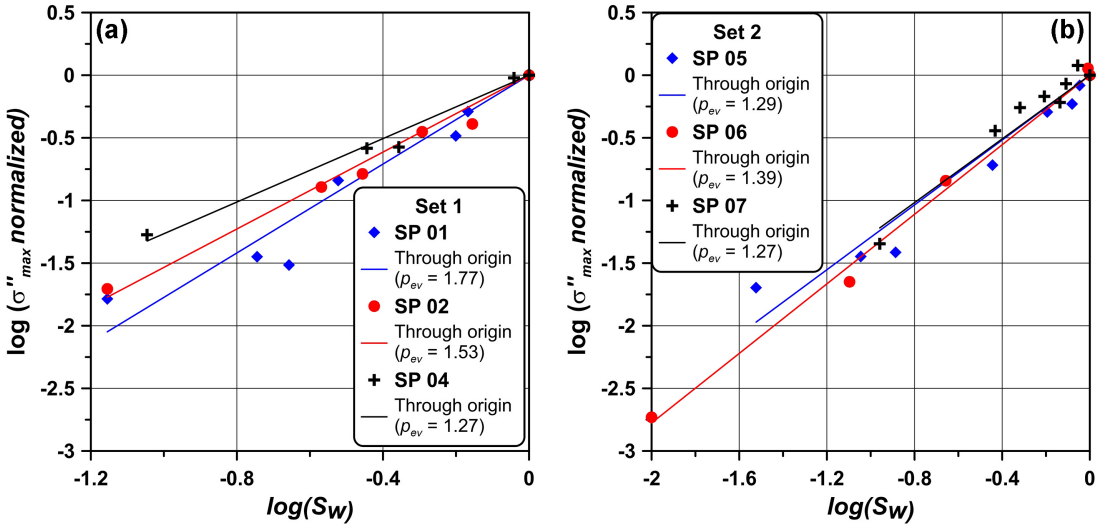

Figure 6. Normalized maximum of imaginary part of conductivity as function of saturation for (a) set 1 samples and (b) set 2 samples.

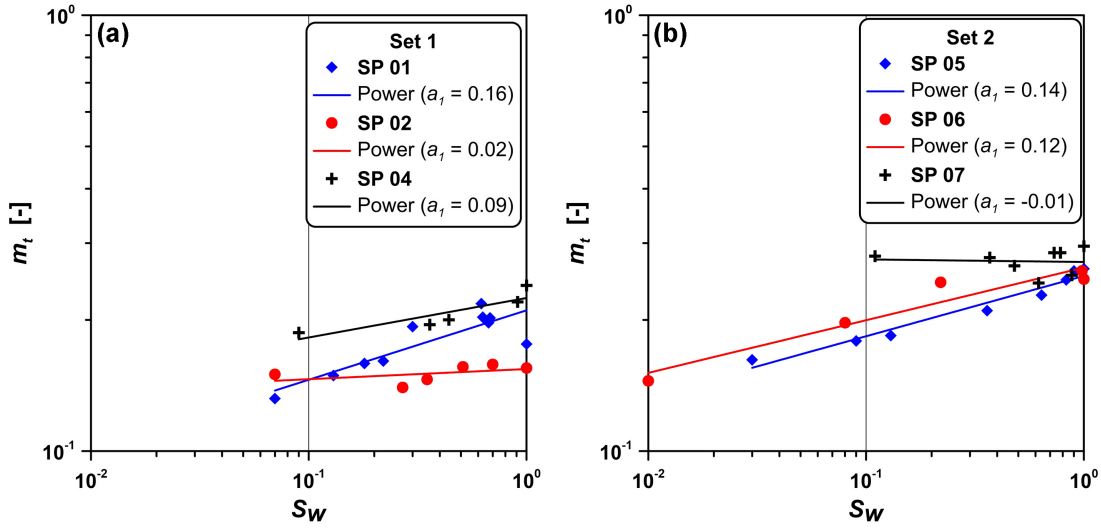

Figure 7. Total chargeability from Debye decomposition as function of saturation for (a) set 1 samples and (b) set 2 samples.

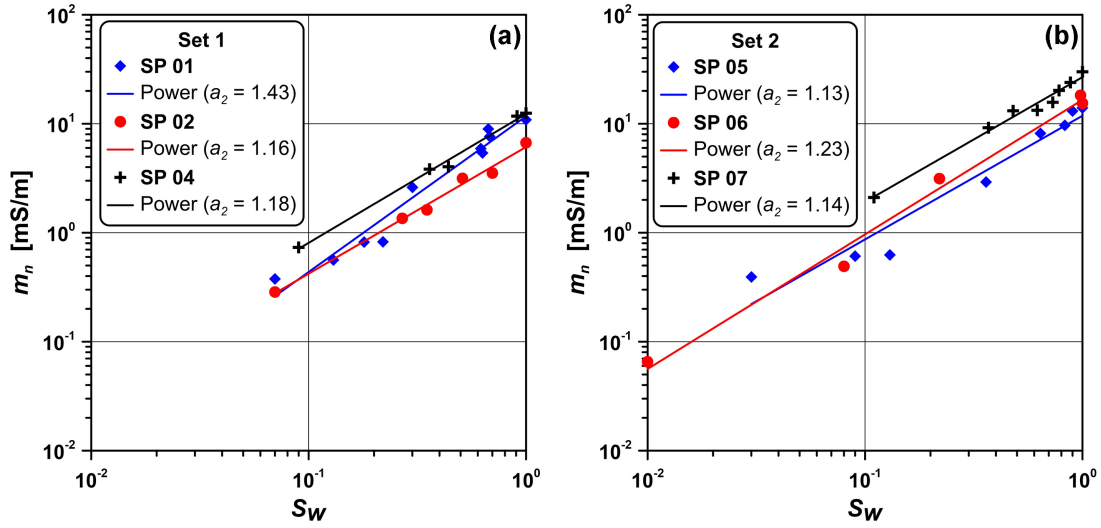

Figure 8. Normalized chargeability as function of saturation for (a) set 1 samples and (b) set 2 samples.

Downloaded from https://academic.oup.com/gji/article/228/1/275/6358528 by Freie Universitaet user on 15 November 2021

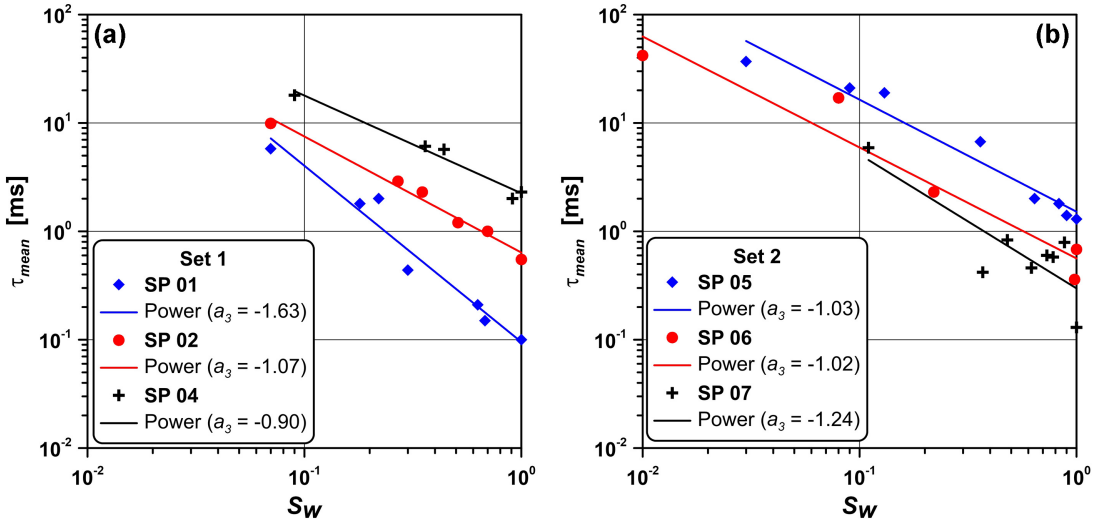

Figure 9. Mean relaxation time as function of saturation for (a) set 1 samples and (b) set 2 samples.

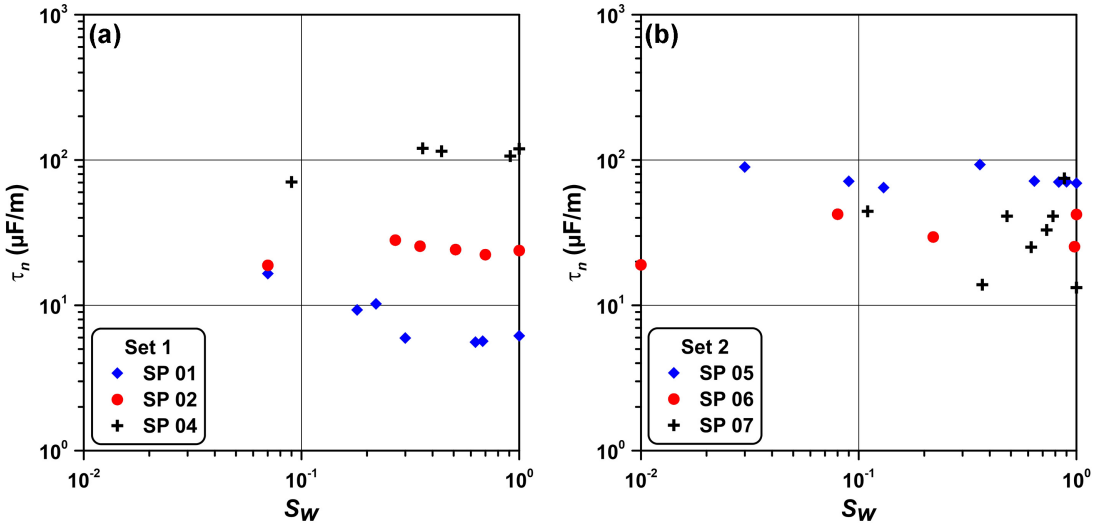

Figure 10. Normalized relaxation time as function of saturation for (a) set 1 samples and (b) set 2 samples.

Table 2. Overview about the IP parameters for all samples at full saturation ($S_w = 1$).

Sample	σ_{gm} [mS m^{-1}]	σ''_{max} [mS m^{-1}]	$f(\sigma''_{max})$ [Hz]	m_t [–]	m_n [mS m^{-1}]	τ_{mean} [ms]	τ_n [μF m^{-1}]	m_P [–]	τ_P [ms]	c [–]
SP 01	61.75	3.92	1995	0.18	10.87	0.10	6.18	0.18	0.10	0.80
SP 02	43.25	2.38	316	0.16	6.7	0.55	23.79	0.16	0.58	0.73
SP 04	51.87	4.48	126	0.24	12.45	2.30	119.3	0.21	2.00	0.83
SP 05	53.29	4.77	251	0.26	13.96	1.30	69.28	0.22	1.10	0.79
SP 06	62.04	5.10	631	0.25	15.89	0.68	42.17	0.25	0.55	0.67
SP 07	101.8	7.61	3162	0.29	30.03	0.14	13.23	-	-	-

Table 3. Overview about the exponents describing the saturation dependence for all samples.

Sample	n_{ev} ($\lvert\sigma\rvert$)	p_{ev} (σ'')	a_1 (m_t)	a_2 (m_n)	a_3 (τ_{mean})
SP 01	1.32	1.77	0.16	1.43	–1.63
SP 02	1.19	1.53	0.02	1.16	–1.07
SP 04	1.06	1.27	0.09	1.18	–0.90
SP 05	1.05	1.29	0.14	1.13	–1.03
SP 06	1.11	1.39	0.12	1.23	–1.02
SP 07	1.17	1.27	–0.01	1.14	–1.24

The chargeability values m_P can be well compared with m_t at all saturation levels. We get a similar good accordance between τ_P and τ_{mean}. The fitting of the Pelton model provides the additional parameter c that characterizes the width of the phase spectra. Fig. 11 demonstrates the decrease in c with increasing width of the grain radius distribution. The graph indicates only the data points of samples with a pyrite content of 5.5 vol. per cent.

Downloaded from https://academic.oup.com/gji/article/228/1/275/6358528 by Freie Universitaet user on 15 November 2021

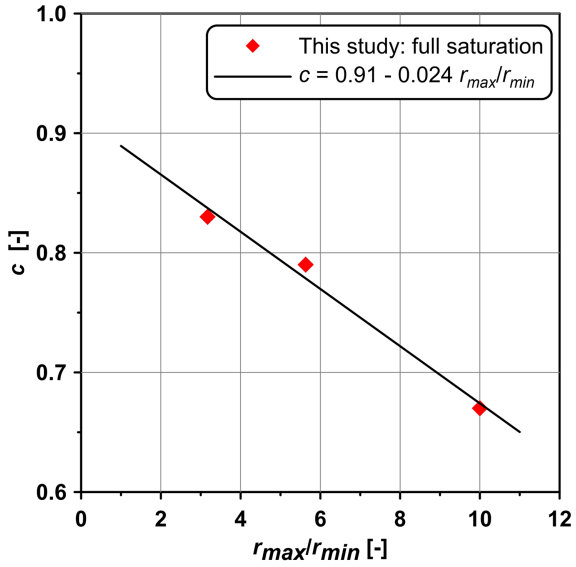

Figure 11. Cole–Cole exponent c as a function of the ratio r_{max}/r_{min}, which quantifies the width of gain radius distribution, for samples SP 04, SP 05 and SP 06 with a uniform pyrite content of 5.5 vol. per cent.

Fig. 12 displays the saturation dependence of the Cole–Cole exponent for both sample sets. We observe a variation of c between 0.34 and 0.83. Most samples indicate a significant decrease of c with gradual desiccation, whereas the c values of sample SP 04 keep the high level for all saturation levels.

DISCUSSION

Spectra

Independent of the grain size and pyrite concentration the real part of conductivity decreases with desiccation. This behaviour, which follows the prediction of the second Archie equation (eq. 2), results from the replacing of the conducting electrolyte by the non-conducting fluid air in the pore space. However, it can be assumed that the salt concentration in the pore water increases while evaporative drying. We observe that the conductivity decrease caused by the increasing air filling is the dominating effect. This observation is in accordance with other studies on evaporative drying (Ulrich & Slater 2004; Kruschwitz 2008; Tartrat *et al.* 2019; Zhang *et al.* 2019).

The spectra of imaginary conductivity indicate a decrease with decreasing saturation at frequencies larger than 1 Hz. We observe not only a strong decrease of σ''_{max} but also a clear shift of the peak frequency $f(\sigma''_{max})$ to lower frequencies. This observation agrees with the desiccation experiments of Tartrat *et al.* (2019). We will discuss these features in more detail later with the parameters of the Debye decomposition.

The phase spectra seem to be dominated by the behaviour of the imaginary part of conductivity. The remarkable decrease in phase amplitude is caused by a stronger decrease of σ''_{max} in comparison with σ' at the same frequency.

Comparing our spectra with the drying experiments on unconsolidated sand samples of Ulrich & Slater (2004), it should be noted that even though their imaginary conductivity decreases as well with desaturation, the phase values increase. Zhang *et al.* (2019) report for their sandstone samples a decrease of both imaginary conductivity and phase amplitude with decreasing saturation. They do not observe any shift of σ''_{max} or phase maximum along the frequency axis during the drying process. The peaks become less accentuated with decreasing saturation. Binley *et al.* (2005) report for their sandstones a clear shift of the phase maximum to higher frequencies as the saturation decreases. According to their explanation, the smaller pore throats dominate the distribution of relaxation times as the larger pores dewater. However, it should be noted that they adopted an experimental approach proposed by Titov *et al.* (2004) that aims at constant water salinity at different saturation levels.

The aforementioned experiments of other studies have been performed with material without metallic particles, whereas the spectral response of our experiments is directly related to variations in the polarization of pyrite particles at different saturation levels. Comparing the complex conductivity spectra of desaturation experiments, we find different characteristics that depend on both the material and the desaturation procedure.

Beside the spectra, we look at special IP parameters that provide more insight into the understanding of the polarization phenomena.

Conductivity amplitude

The saturation exponents n_{ev} of the conductivity amplitudes vary in a small range with values being slightly larger than one. Though we find the largest value with $n_{ev} = 1.32$ for the sample SP 01 with the smallest grain radius of pyrite particles, a significant dependence of n_{ev} on pyrite content and grain size cannot be identified. The resulting exponents are comparable with the values determined by Ulrich & Slater (2004) for their unconsolidated material. Obviously, the addition of a small volume of pyrite to unconsolidated material does not affect the saturation dependence of conductivity amplitude. Zhang *et al.* (2019) report for their sandstone samples saturation exponents $n_{ev} < 1$. Tartrat *et al.* (2019) identify similarly low values for their illitic clay samples. Their findings suggests that the saturation exponent n_{ev} decreases with increasing clay content.

Maximum of imaginary part of conductivity

The imaginary part of conductivity shows a strong dependence on saturation. The saturation exponents p_{ev} vary between 1.27 and 1.77. Again, sample SP 01 with the smallest grain radius of pyrite particles indicates the largest value with $p_{ev} = 1.77$.

The exponents p_{ev} of our study are higher than in the experiments on unconsolidated material without electronically conductive particles reported by Ulrich & Slater (2004). Considering the different origin and size of polarization, a comparison between the saturation exponents p_{ev} is not very instructive.

Total chargeability

The desiccation experiments on sandstones have shown a clear decrease of total chargeability with decreasing water saturation (Zhang *et al.* 2019). In contrast, for our experiments with sand–pyrite mixtures, the total chargeability m_t indicates only a weak dependence on saturation. Other experiments, using mixtures with metallic particles, report for varying grain size or changing water conductivity a minor influence on total chargeability (e.g. Pelton *et al.* 1978; Gurin *et al.* 2015; Revil *et al.* 2015a; Hupfer *et al.* 2016). However, all these experiments indicate a major dependence of total chargeability on the volumetric content of metallic particles as predicted by eqs (13) and (14). Our experiments confirm a moderate increase in total chargeability for the samples with 5.50 vol. per

Downloaded from https://academic.oup.com/gji/article/228/1/275/6358528 by Freie Universitaet user on 15 November 2021

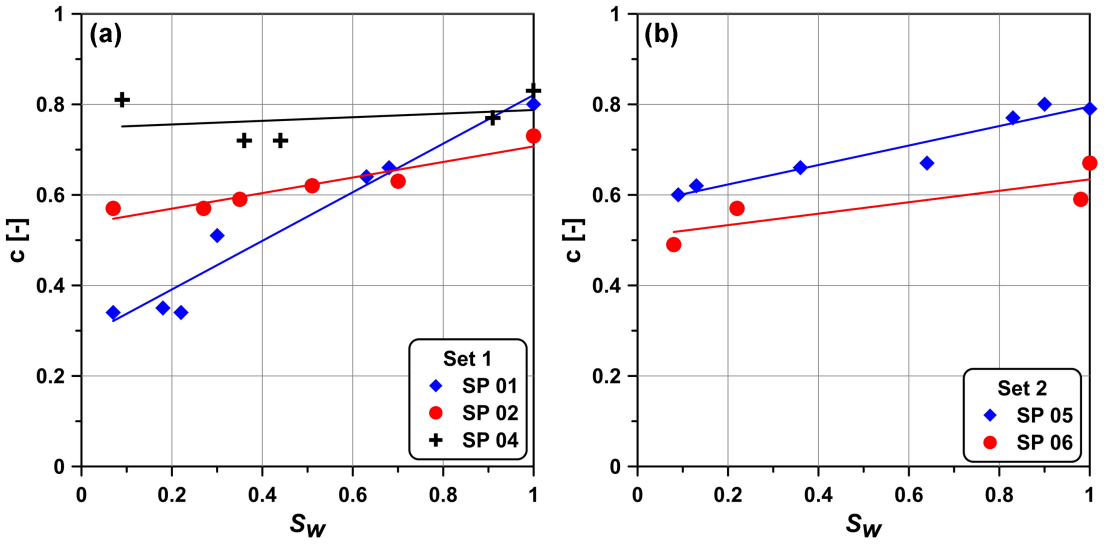

Figure 12. Cole–Cole exponent c as a function of saturation for (a) sample set 1 and (b) sample set 2.

cent in comparison to the samples with only 2.75 vol. per cent pyrite. However, the measured values deviate from the predictions of eqs (13) and (14). The resulting total chargeability of the samples with lower p_v (SP 01 and SP 02, see Table 2) overestimate the theoretical values ($m_t = 0.125$ for eq. (13) with $m_m = 0.01$). The relative overestimation reduces for the samples with 5.50 vol. per cent. Eq. (13) predicts $m_t = 0.225$ for these samples. We observe a similar difference between the measured and predicted $\varphi_{\max}$ where eq. (15) predicts a phase maximum of $\varphi_{\max} = 124$ mrad for the samples with 5.50 vol. per cent.

The relationships between p_v and m_t (eqs 13 and 14) as well as between p_v and $\varphi_{\max}$ (eq. 15) describe the general trend in a qualitative way. However, our data demonstrate that the eqs (13) to (15) cannot be used for a reliable quantitative prediction of the volumetric content of metallic particles in pyrite–sand mixtures.

Normalized chargeability

The normalized chargeability m_n is the product of total chargeability and the conductivity σ_{gm} (eq. 10). Because the total chargeability seems to be unaffected by saturation, it is obvious that the normalized chargeability reflects the saturation dependence of the conductivity. Therefore, Figs 5 and 8 indicate similar power-law exponents for the saturation dependence of conductivity and normalized chargeability.

The metal factor, which is proportional to m_n, has been proposed in mineral exploration for the determination of the metal content ores. Considering the findings of this study, the total chargeability seems to be a better quantity for the estimation of metal content. Both quantities normalized chargeability and metal factor are strongly affected by water saturation.

The normalized chargeability is regarded as parameter that quantifies the polarization magnitude regardless of the background conductivity. In the case of flat spectra of imaginary conductivity, normalized chargeability is proportional to the average imaginary conductivity (e.g. Shuey & Johnson 1973). Therefore, the comparison of the saturation exponents from $\sigma''_{\max}$ (Fig. 6) and normalized chargeability (Fig. 8) indicates minor differences. The exponent p_{ev} is between 1.27 and 1.77 and comparable to the exponent a_2 that varies between 1.13 and 1.43.

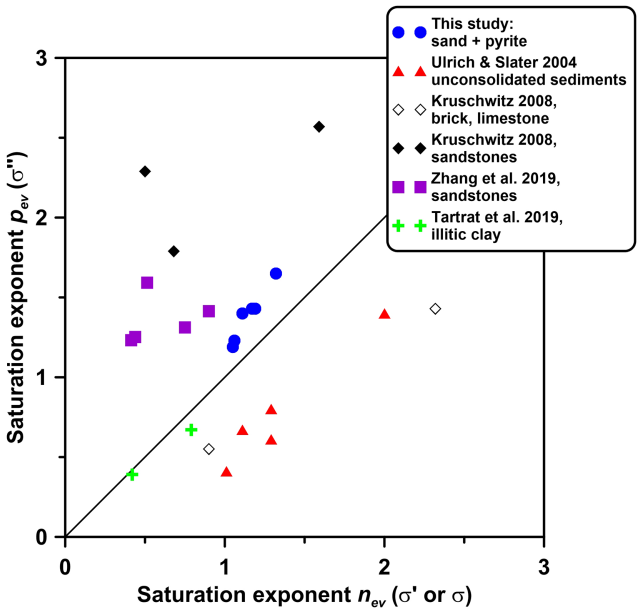

Figure 13. Saturation exponents from real and imaginary part of conductivity and comparison with the results from other studies.

Saturation exponents

Fig. 13 compares the saturation exponents from conduction (n_{ev}) and polarization (p_{ev}) for samples of different studies that have been desaturated by evaporative drying. We observe a wide variation of the saturation exponents n_{ev} and p_{ev} between 0.4 and 2.6. Considering the salinity increase while evaporative drying, lower saturation exponents n_{ev} are expected in comparison with the Archie saturation exponent n (eq. 2) resulting from flushing experiments with no change in water conductivity. The exponents n_{ev} determined for the sand–pyrite mixtures prove to be lower than the classical Archie saturation exponent with $n \approx 2$ for both unconsolidated and consolidated sediments (e.g. Ulrich & Slater 2004; Schön 2011).

Vinegar & Waxman (1984) predict for the saturation exponents of flushing experiments on sandstones the relationship $p = n–1$. This relationship is not confirmed by evaporative drying experiments.

Downloaded from https://academic.oup.com/gji/article/228/1/275/6358528 by Freie Universitaet user on 15 November 2021

However, we do not observe any other fixed relationship between n_{ev} and p_{ev}. Considering that the saturation exponent n_{ev} is more related to the volume conductivity (electrolytic conductivity inside the pore space) and p_{ev} to the surface conductivity (conductivity and polarization in the electrical double layer), the relationship $n_{ev} = p_{ev}$ assumes a uniform decrease of both volume and surface conductivity during the evaporative drying process. Fig. 13 indicates a remarkable variation in the differences between the two saturation exponents.

The data points of our sand–pyrite mixtures are located together with sandstone samples investigated by Kruschwitz (2008) and Zhang *et al.* (2019) above the diagonal line in the diagram of Fig. 13. The relationship $p_{ev} > n_{ev}$ indicates a stronger effect of evaporative drying on surface conductivity. We recognize that the data points of other samples, which are located below the diagonal line, indicate a different behaviour with $p_{ev} < n_{ev}$. We find in this group unconsolidated sands (Ulrich & Slater 2004), illitic clay samples (Tartrat *et al.* 2019) and a historic brick and a limestone sample (Kruschwitz 2008). These samples are characterized by a stronger effect of desiccation on volume conductivity. A theoretical approach that assumes equal saturation exponents for both volume and surface conductivity does not reflect the variability of the relationships between p_{ev} and n_{ev}. Beside the mineral composition, the distribution and the salinity of the conducting fluid control the saturation exponent. The general topology of the liquid phase depends on the rock texture, the wetting properties of the minerals and the saturation history (e.g. Knight 1991). Therefore, the prediction of saturation exponents is a challenging task.

Mean relaxation time

The mean relaxation time reveals a strong dependency on the saturation and decreases with increasing saturation. This behaviour is in contrast to the findings of Binley *et al.* (2005) and Zhang *et al.* (2019), who observed an increase of relaxation time with increasing saturation on their sandstone samples. In contrast to Zhang *et al.* (2019), who could not observe a significant frequency shift of the maximum phase amplitude, the results of Binley *et al.* (2005) do show a clear shift to higher frequencies with decreasing saturation. Our results, however, show a clear shift to lower frequencies with desaturation. Obviously, the prevailing polarization phenomena cause the different behaviour of sandstones and sand–pyrite mixtures.

Several experimental studies have shown that the grain size of the conducting particles control the relaxation time (Pelton *et al.* 1978; Mahan *et al.* 1986; Revil *et al.* 2015b). Our experiment verifies the pyrite grain size dependence of the relaxation time. The larger the mean pyrite grain radius (Table 1) the larger the relaxation time. In the case of mixtures with two pyrite grain radii (set 2), we observe that the mean relaxation time is dominated by fraction of the smaller grain radius. This effect becomes obvious if we compare the mean relaxation times of samples SP 01 and SP 07 at full water saturation. The two samples contain 2.75 vol. per cent of pyrite with the grain radius fraction 56 to 100 µm. Additionally, sample SP 07 contains another 2.75 vol. per cent of the large grain radius fraction 500–1000 µm. Although the resulting mean grain radius of sample SP 07 is considerably larger (see Table 1), we find only a slight increase in the mean relaxation time from 0.10 to 0.14 ms (Table 2).

Several studies on mixtures with metallic particles report a decrease of relaxation time with increasing water conductivity (e.g. Slater *et al.* 2005; Gurin *et al.* 2015; Hupfer *et al.* 2016; Revil *et al.* 2018; Feng *et al.* 2020). As the result of evaporative drying, the volume of water in the pore space decreases. However, the amount of dissolved salt in the pore water will not change. Therefore, the salt concentration increases proportionally to the inverse of saturation. Following the findings of the above-mentioned studies and considering eq. (17), we should observe a decrease of relaxation time with gradual desaturation of our mixtures. However, we observe the opposite trend. Thus, the increase in water conductivity cannot be the major controlling effect of the observed change in relaxation time. We attribute the increase in relaxation time to the general increase in sample resistivity during the drying process as predicted by the conceptional model with eq. (20).

Normalized relaxation time

According to the definition in eq. (10), the normalized relaxation time τ_n corresponds to the ratio of mean relaxation time and mean resistivity of the sample. The normalized relaxation time does not show any significant dependence on water saturation (Fig. 10) because the approximately linear decrease of the mean relaxation time with increasing saturation (Fig. 9) compensates the approximately linear increase of conductivity (Fig. 5).

A variety of experiments has been performed to investigate the influence of water salinity on relaxation time of mixtures with conductive particles (e.g. Slater *et al.* 2005; Gurin *et al.* 2015; Hupfer *et al.* 2016; Revil *et al.* 2018; Feng *et al.* 2020). The experiments confirm a linear relationship between relaxation time and water resistivity. Considering the proportionality between the water resistivity ρ_w and the resistivity of the fully water saturated sample ρ_b with low surface conductivity ($\rho_w = \frac{\rho_b}{F}$, with F being the formation factor) an increase of water resistivity causes an increase of ρ_b and finally an increase in relaxation time as predicted by eq. (20).

Revil *et al.* (2017) present an investigation on mixtures consisting of sand, bentonite and pyrite with fixed volume percentage and grain size. They found a proportionality between relaxation time and the resistivity of the background material, which decreases with increasing bentonite content. Their experimental finding is also in agreement with eq. (20).

As demonstrated by our experiment, the evaporative drying causes an increase in sample resistivity. Again, this resistivity increase causes an increase in relaxation time as predicted by eq. (20).

All the mentioned experiments confirm that the resistivity of the embedding material controls the discharge of the conductive particles of uniform grain size. On the other hand, the grain size or the active surface of the conductive particles control the 'specific capacitance' c_s of the medium. It is known that the capacity of a spherical condenser increases linearly with its radius (Tipler & Mosca 2003). Considering the relationship in eq. (20), an increasing c_s increases the relaxation time as well. Therefore, it is expected that in the case of constant resistivity of the embedding material the relaxation time increases with increasing grain size as a variety of experiments has demonstrated (e.g. Pelton *et al.* 1978; Nordsiek & Weller 2008; Revil *et al.* 2015b).

Gurin *et al.* (2019) showed that a partial passivation of the metallic surfaces by electrical isolation causes a decrease in relaxation time. Considering that the passivation decreases chargeable surface of the particles and thereby the capacity of the metallic particles, the experimental results confirm as well the conceptional model (eq. 20).

Downloaded from https://academic.oup.com/gji/article/228/1/275/6358528 by Freie Universitaet user on 15 November 2021

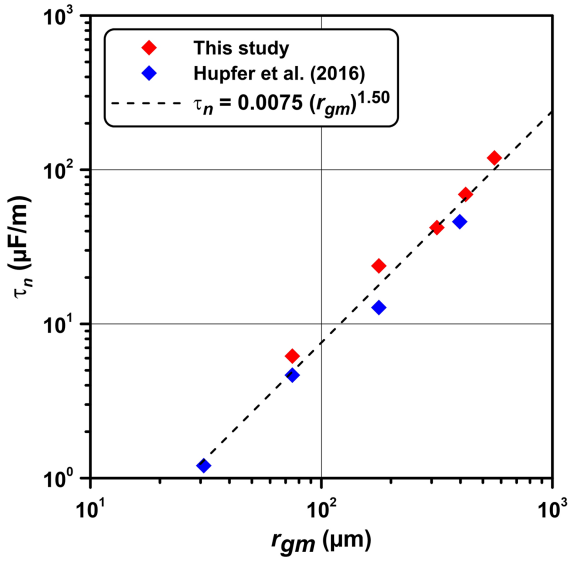

Figure 14. Normalized relaxation time as a function of function of the mean grain radius r_{gm} for sand–pyrite mixtures with a volume-percentage of pyrite between 2.75 er cent. Data originate from Hupfer *et al.* (2016) and from this study.

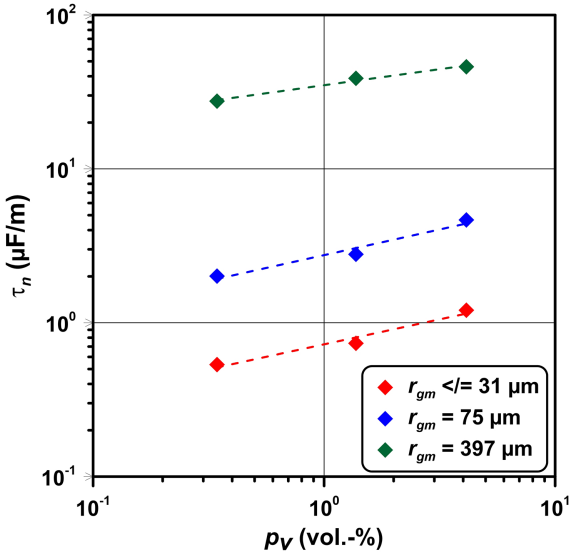

Figure 15. Normalized relaxation time as a function of pyrite content for sand–pyrite mixtures with varying mean grain radii. Data originate from Hupfer *et al.* (2016).

Our study, together with earlier experiments on pyrite–sand mixtures of Hupfer *et al.* (2016), confirm that the size and content of pyrite particles control the physical quantity $c_s = \tau_n$. The graph in Fig. 14 indicates a power-law relationship with an exponent of 1.5 between the mean grain radius of the pyrite particles and the quantity τ_n. The resulting exponent is larger than one as predicted for models assuming spherical condensers but smaller than two as expected for models based on diffusion processes (Schwarz 1962; Revil *et al.* 2015a).

Feng *et al.* (2020) found for their experiments, using gold coated spheres or stainless-steel spheres with varying radius *r,* a linear relationship between the normalized relaxation time and radius ($\tau_n = r\ C_0$, where C_0 denotes the surface specific capacitance in F m^{-2}). Other studies identified larger power-law exponents of *r*. Nordsiek & Weller (2008) report an exponent of 1.54 for the relationship between mean relaxation time and the diameter of slag grains in a mixture. Gurin *et al.* (2013) determined an exponent of 1.73 for their sand–ore mixtures. Most experiments have been performed using crushed particles with irregular shapes and surfaces (see Fig. 1c). We assume that the exponent is related to the shape and surface topology of the metallic particles. Obviously, rough surfaces or fractal surface structures cause exponents that differ from the one of ideally spherical particles.

Fig. 15 displays the relationship between pyrite content and the quantity τ_n for three mixtures with a single grain size fraction based on the data of Hupfer *et al.* (2016). We observe a slight increase of τ_n with increasing pyrite content with power-law exponents close to 0.3. Up to now, we are not able to provide a theoretical explanation for the resulting power-law exponents. More experiments are required to confirm our findings and to reveal other dependences.

Cole–Cole exponent

Our experiment confirm that the Cole–Cole exponent *c* of the double Pelton model (eq. 12) is related to the width of the grain size distribution. Fig. 11 shows the expected decrease of *c* with an increasing ratio r_{max}/r_{min}, which quantifies the width of the grain size distribution, for samples with the same pyrite content.

We demonstrate in Fig. 12 experimental evidence for a saturation dependence of the Cole–Cole exponent *c*. A strong dependence is observed for sample SP 01 with the smallest mean grain radius of pyrite particles (75 µm). The exponent decreases from $c = 0.8$ at full saturation to a value of $c = 0.34$ at $S_w = 0.07$. The saturation dependence of *c* decreases for sample SP 02 with a mean grain radius of 177 µm and disappears for sample SP 04 with the largest mean grain radius (561 µm). Tartrat *et al.* (2019) found for their clay–pyrite mixtures that *c* is independent of saturation. Considering that they used pyrite particles with radii larger than 1000 µm, this finding is in accordance with our experiments. However, a generalization of the independence of *c* on S_w is not justified as demonstrated in our experiments with smaller grain radii. On the other hand, the experiments of Tartrat *et al.* (2019) show evidence for an increase of *c* with increasing pyrite content (their Fig. 17). The smaller values of *c* for their experiment might be attributed to the higher chargeability of the background material.

CONCLUSIONS

We observed that metallic particles do not severely affect the drying process of the unconsolidated material. The conductivity decrease during the evaporative drying process can be well approximated by a power law as described by the second empirical Archie equation. The resulting saturation exponent n_{ev} with values slightly larger than one corresponds to unconsolidated sands without metallic particles. We also found that desaturation affects real and imaginary part of conductivity in a similar degree. A power law describes the saturation dependence of the maximum of the imaginary part of conductivity. The resulting saturation exponent p_{ev} is only slightly higher than the exponent of the real part of conductivity n_{ev}.

The Debye decomposition algorithm provides useful IP parameters for the evaluation of the desaturation process. The total chargeability does not indicate any significant trend during evaporative

Downloaded from https://academic.oup.com/gji/article/228/1/275/6358528 by Freie Universitaet user on 15 November 2021

drying. This observation is in good agreement with those models that relate chargeability to the volumetric metal content in the sample. In contrast, a strong decrease of φ_{max} with increasing desaturation could be observed. Therefore, the total chargeability is the preferred parameter for an evaluation of metal content. The relationship between normalized chargeability and water saturation indicates a power-law relationship. The exponents are similar to p_{ev} resulting for the imaginary part of conductivity.

The mean relaxation time, which is another parameter provided by the Debye decomposition, indicates a clear increase during the desaturation process. Previous models attributed an increase in relaxation time to a decrease in water salinity. However, the evaporative drying causes an increase of water conductivity. Therefore, the experimental findings require a review of the existing models.

The proposed conceptional model compares a mixture of pyrite particles in an embedding material with the behaviour of an electrical RC circuit. Each pyrite grain acts as small condenser that is charged and discharged via the conductive background material. According to this physical model, the relaxation time is proportional to the resistivity of the background material. The resistivity increase during evaporative drying causes an increase of relaxation time as observed in our experiments. This conceptional model is also in good agreement with other experiments that are related to a change in background resistivity by varying the water conductivity or the clay content in the fully water saturated sample. The normalized relaxation time, with the physical unit F m^{-1}, proves to be a suitable parameter to describe the capacitive behaviour of the dispersed pyrite particles. We observe a power-law relationship with an exponent 1.5 between normalized relaxation time and grain size of the pyrite particles. Additionally, an increase in volumetric pyrite content causes an increase of normalized relaxation time as well.

The desaturation experiments with sand–pyrite mixtures provide more insight into the polarization phenomena of particles with electronically conductive (metallic) particles. The findings are important for the application of the SIP method as tool for the evaluation of the remaining ore content in mining dumps.

ACKNOWLEDGEMENTS

The experimental work was done within the master thesis from LB. All the experiments were conducted in the laboratories at the Federal Institute for Geosciences and Resources (BGR), Germany. We hereby acknowledge the help from the BGR colleagues Ursula Noell, Stephan Costabel and the technical staff . The thesis work was part of the ROBEHA project, which was funded by the BMBF (German Ministry of Education and Research, grant 033R105). AW acknowledges the support of DFG through grant no. WE 1557/17–1.

DATA AVAILABILITY STATEMENT

The data underlying this paper will be shared on reasonable request to the corresponding author.

REFERENCES

Anterrieu, O., Chouteau, M. & Aubertin, M., 2010. Geophysical characterization of the large-scale internal structure of a waste rock pile from a hard rock mine. *Bull. Eng. Geol. Environ.,* **69,** 533–548.

Binley, A., Slater, L.D., Fukes, M. & Cassiani, G., 2005. Relationship between spectral induced polarization and hydraulic properties of saturated and unsaturated sandstone, *Water Resour. Res.,* **41,** W12417, doi:10.1029/2005WR004202.

Bleil, D.F., 1953. Induced polarization: a method of geophysical prospecting. *Geophysics,* **18,** 636–661.

Feng, L., Li, Q., Cameron, S.D., He, K., Colby, R., Walker, K.M., Deckman, H.W. & Ertaş, D., 2020. Quantifying induced polarization of conductive inclusions in porous media and implications for geophysical measurements. *Sci. Rep.,* **10,** 1669.

Grissemann, C., Furche, M., Noell, U., Rammlmair, D., Günther, T. & Baen, A.J.R., 2007. Geoelectrical observations at the mining dumps of the Peña de Hierro copper mine in the Rio Tinto mining district/Spain, in *Proceedings of the 10th International Congress of the Brazilian Geophysical Society,* Brazil.

Gurin, G., Tarasov, A., Ilyin, Yu. & Titov, K., 2013. Time domain spectral induced polarization of disseminated electronic conductors: laboratory data analysis through the Debye decomposition approach, *J. appl. Geophys.,* **98,** 44–53.

Gurin, G., Titov, K. & Ilyin, Y., 2019. Induced polarization of rocks containing metallic particles: evidence of passivation effect. *Geophys. Res. Lett.,* **46,** 670–677.

Gurin, G., Titov, K., Ilyin, Y. & Tarasov, A., 2015. Induced polarization of disseminated electronically conductive minerals: a semi-empirical model, *Geophys. J. Int.,* **200**(3), 1555–1565.

Hupfer, S., Martin, T., Weller, A., Kuhn, K., Günther, T., Djotsa, V. & Noell, U., 2016. Polarization effects of unconsolidated sulphide-sand-mixtures, *J. appl. Geophys.,* **135,** 456–465.

Knight, R., 1991. Hysteresis in the electrical resistivity of partially saturated sandstones, *Geophysics,* **56**(12), 2139–2147

Kruschwitz, S., 2008, Assessment of the complex resistivity behavior of salt affected building materials, *PhD thesis*, Technical University Berlin, Germany.

Kuhn, K. & Meima, J.A., 2019. Characterization and economic potential of historic tailings from gravity separation: implications from a mine waste dump (Pb-Ag) in the Harz mountains mining district, Germany, *Minerals,* **9,** 303.

Lesmes, D.P. & Frye, K.M., 2001. The influence of pore fluid chemistry on the complex conductivity and induced-polarization responses of Berea sandstone. *J. geophys. Res.,* **106,** 4079–4090.

Mahan, M.K., Redman, J.D. & Strangway, D.W., 1986. Complex resistivity of synthetic sulfide bearing rocks. *Geophys. Prospect.,* **34,** 743–768.

Martin, T., 2010. Complex resistivity measurements on oak. *Eur. J. Wood Prod.,* **70,** 45–53.

, Günther, T., Weller, A., Kuhn, K.Martin, T., 2021. Classification of slag material by spectral induced polarization laboratory and field measurements, *J. appl. Geophysics,* **194**(104439.

Martin, T., Kuhn, K., Günther, T. & Kniess, R., 2020. Geophysical exploration of a historical stamp mill dump for the volume estimation of valuable residues, *J. Environ. Eng. Geophys.,* **25,** 275–286.

Martin-Crespo, T., Martin-Velázquez, S., Gómez-Ortiz, D., De Ignacio-San José, C. & Lillo-Ramos, J., 2011. A geochemical and geophysical characterization of sulfide mine ponds at the Iberian Pyrite Belt (Spain). *Water Air Soil Pollut.,* **217,** 387–405.

Nordsiek, S. & Weller, A., 2008. A new approach to fitting induced-polarization spectra, *Geophysics,* **73**(6), F235–F245.

Pelton, W.H., Ward, S.H., Hallof, P.G., Sill, W.R. & Nelson, P.H., 1978. Mineral discrimination and removal of inductive coupling with multifrequency IP. *Geophysics,* **43,** 588–609.

Placencia-Gomez, E., Parviainen, A., Hokkanen, T. & Loukola-Ruskeeniemi, K., 2010. Integrated geophysical and geochemical study on AMD generation at the Haveri Au–Cu mine tailings, SW Finland. *Environ. Earth Sci.,* **61,** 1435–1447.

Poggendorf, C., Rüpke, A., Gock, E., Saheli, H., Kuhn, K. & Martin, T., 2015. Nutzung des Rohstoffpotentials von Bergbau- und Hüttenhalden am Beispiel des Westharzes, in *Mineralische Nebenprodukte und Abfälle 2—Aschen, Schlacken, Stäube und Baurestmassen,* pp. 580–602, ed. Thomé-Kozmiensky, K.J., TK Verlag.

Revil, A., Abdel Aal, G.Z., Atekwana, E.A., Mao, D. & Florsch, N., 2015b. Induced polarization response of porous media with metallic particles — Part 2: comparison with a broad database of experimental data. *Geophysics,* **80**(5), D539–D552.

Downloaded from https://academic.oup.com/gji/article/228/1/275/6358528 by Freie Universitaet user on 15 November 2021

Revil, A., Coperey, A., Mao, D., Abdulsamad, F., Ghorbani, A., Rossi, M. & Gasquet, D., 2018. Induced polarization response of porous media with metallic particles — Part 8: influence of temperature and salinity. *Geophysics,* **83**(6), E435–E456.

Revil, A., Florsch, N. & Mao, D., 2015a. Induced polarization response of porous media with metallic particles— Part 1: a theory for disseminated semiconductors. *Geophysics,* **80**(5), D525–D538.

Revil., A., Sleevis, M.F. & Mao, D., 2017. Induced polarization response of porous media with metallic particles — Part 5: influence of the background polarization. *Geophysics,* **82**(2), E77–E96.

Rucker, D.F., Glaser, D.R., Osborne, T. & Maehl, W.C., 2009. Electrical resistivity characterization of a reclaimed gold mine to delineate acid rock drainage pathways. *Mine Water Environ.,* **28,** 146–157.

Schön, J.H., 2011, *Physical Properties of Rocks: A Workbook,* Elsevier.

Schwarz, G., 1962, A theory of the low-frequency dielectric dispersion of colloidal particles in electrolyte solution. *J. Chem. Phys.,* **66,** 2636–2642.

Shuey, R.T. & Johnson, M., 1973. On the phenomenology of electrical relaxation in rocks, *Geophysics,* **38,** 37–48.

Slater, L., Choi, J. & Wu, Y., 2005. Electrical properties of iron-sand columns: implications for induced polarization investigations and performance monitoring of iron-wall barriers. *Geophysics,* **70,** G87–G94.

Tartrat, T., Revil, A., Abdulsamad, F., Ghorbani, A., Jougnot, D., Coperey, A., Yven, B. & de La Vaissière, R., 2019. Induced polarization response of porous media with metallic particles — Part 10: influence of desiccation. *Geophysics,* **84**(5), E357–E375.

Tipler, P. & Mosca, G., 2003. *Physics for Scientists and Engineers,* 5th edn, pp. 752, Macmillan, ISBN 978-0-7167-0810-0.

Titov, K., Kemna, A., Tarasov, A. & Vereecken, H., 2004. Induced polarization of unsaturated sands determined through time-domain measurements. *Vadose Zone J.,* **3,** 1160–1168.

Ulrich, C. & Slater, L.D., 2004. Induced polarization measurements on unsaturated, unconsolidated sands. *Geophysics,* **69**(3), 762–771.

Van Voorhis, G., Nelson, P. & Drake, T., 1973. Complex resistivity spectra of porphyry copper mineralization. *Geophysics,* **38,** 49–60.

Vinegar, H.J. & Waxman, M.H., 1984, Induced polarization of shaly sands. *Geophysics,* **49,** 1267–1287.

Wong, J., 1979, An electrochemical model of the induced-polarization phenomenon in disseminated sulfide ores, *Geophysics,* **44,** 1245–1265.

Zhang, Z., Weller, A., Kruschwitz, S. & Nordsiek, S., 2019. Effect of evaporative drying on complex conductivity spectra of sandstones. *Geophysics,* **84**(1), MR61–MR72.

Zimmermann, E., Kemna, A., Berwix, J., Glaas, W., Münch, H. & Huisman, J., 2008. A high-accuracy impedance spectrometer for measuring sediments with low polarizability. *Meas. Sci. Technol.,* **19,** doi:10.1088/0957-0233/19/9/094010.

Downloaded from https://academic.oup.com/gji/article/228/1/275/6358528 by Freie Universitaet user on 15 November 2021